Applied Physics Letters

Through-skin pilot-hole detection and localization with a mechanically translatable atomic magnetometer

Cite as: Appl. Phys. Lett. **120**, 014002 (2022); https://doi.org/10.1063/5.0081274
Submitted: 08 December 2021 • Accepted: 23 December 2021 • Published Online: 05 January 2022

Benjamin Maddox, Yuval Cohen and Ferruccio Renzoni

View Online Export Citation CrossMark

QBLOX

1 qubit

Shorten Setup Time
Auto-Calibration
More Qubits

Fully-integrated
Quantum Control Stacks
Ultrastable DC to 18.5 GHz
Synchronized <<1 ns
Ultralow noise

100s qubits

visit our website >

© 2022 Author(s).

Applied Physics Letters ARTICLE scitation.org/journal/apl

Through-skin pilot-hole detection and localization with a mechanically translatable atomic magnetometer

Cite as: Appl. Phys. Lett. **120**, 014002 (2022); doi: 10.1063/5.0081274
Submitted: 8 December 2021 · Accepted: 23 December 2021 ·
Published Online: 5 January 2022

View Online Export Citation CrossMark

Benjamin Maddox, Yuval Cohen, and Ferruccio Renzoni[a)]

AFFILIATIONS

Department of Physics and Astronomy, University College London, Gower Street, London WC1E 6BT, United Kingdom

[a)]Author to whom correspondence should be addressed: f.renzoni@ucl.ac.uk

ABSTRACT

We demonstrate through-skin electromagnetic induction imaging of pilot-holes in an aluminum block concealed by a 0.41 mm thick aluminum shield with a 1.49 kg mechanically translatable radio frequency atomic magnetometer. The pilot-holes are identified and localized with submillimeter accuracy both with and without the Al shield. We utilize a dual-frequency technique to isolate the image of the target while removing the effect of the shielding from the image. Imaging accuracy is shown to be robust in a range of different operating conditions and immune to the effect of a thermal insulator between the shielding and the target. The approach introduced here finds direct application in aircraft wing manufacture and is competitive with existing approaches.

© 2022 Author(s). All article content, except where otherwise noted, is licensed under a Creative Commons Attribution (CC BY) license (http://creativecommons.org/licenses/by/4.0/). https://doi.org/10.1063/5.0081274

A common problem in several manufacturing processes is the anchoring of a metal panel to a support structure. For example, in aircraft wing assembly, the wing outer "skin" must be fixed to anchoring points on the thick strut. The challenge in this process is the precise identification of the anchoring points without visual access. These anchoring points are often pilot-holes, which are pre-drilled in the thick strut. Different solutions have been put forward for this. Transient-pulsed thermography was found to be able to penetrate the skin and reveal the position of the pilot-holes, although any thermal resistance between skin and strut significantly decreases the image contrast.[1] An alternative approach consists in introducing permanent magnets in the pilot-holes and then determining their location via magnetic measurements.[2] While effective, the procedure requires access to both sides of the skin, causing a significant increase in manufacturing time and cost. In this work, we put forward an approach to pilot-hole detection that does not rely on thermal excitation nor requires access to both sides of the skin, thus overcoming some limitations of the current approaches. Our approach relies on electromagnetic induction imaging (EMI) with radio frequency atomic magnetometers (RF-AMs)[3,4] and a dedicated procedure for the extraction of through-skin images with high contrast. As RF-AMs retain extreme sensitivity at low-frequency,[5–7] it is possible to penetrate the shield by lowering the operating frequency of the sensor and imaging the concealed structure behind the shield. Our implementation involves the translation of the RF-AM over the area of interest and, thus, is directly applicable to the scanning of a large static structure in an industrial situation.

The EMI apparatus is described and characterized in detail in a previous publication[8] with a brief description in the following. The sensor consists of a mechanically translatable RF-AM weighing 1.49 kg with dimensions $110 \times 110 \times 145\ \mathrm{mm}^3$ (W × L × H). The housing of the sensor is 3D printed nylon, providing structural support and placement for all necessary components. Vertical cavity surface-emitting lasers (VCSELs), magnetic field compensation coils, vapor cell, and polarimeter are all included in the sensor head, without external optical input or output. The sensor is moved using a motorized 2D mechanical translational stage. Figure 1 shows a simplified view of the complete setup. A cubic ^{87}Rb vapor cell ($20 \times 20 \times 20\ \mathrm{mm}^3$) with 20 Torr of N_2 buffer gas and no cell wall coating sits at the center of the sensor head. The circularly polarized pump beam, resonant with the D_1 $F = 1 \rightarrow F'$ transition, propagates through the cell in the $\hat{x}$ direction, aligned with a static bias magnetic field $\mathbf{B}_{Bias}$. The σ^+ pump light transfers the ^{87}Rb atoms from the $F=1$ state to the F' states where they can de-excite to either ground state. Over many cycles, this leads to the depopulation of $F=1$ and a build-up of atoms in the stretched $|F = 2, m_F = 2\rangle$ state, which is dark to the pump. $\mathbf{B}_{Bias}$ is

© Author(s) 2022

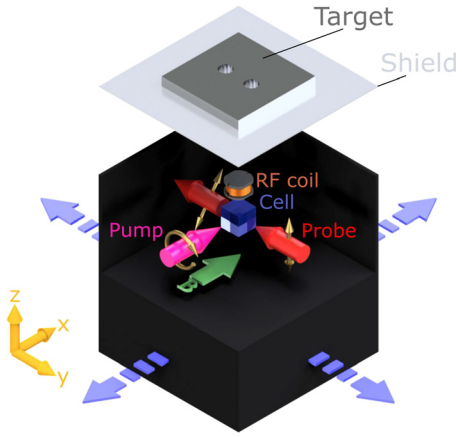

FIG. 1. Simplified cross-sectional schematic of the mechanically translatable atomic magnetometer (not to scale) and its geometry with respect to the shielded target. The sensor head is mounted on a 2D translational stage and can be moved in the *x*-*y* plane. Golden arrows illustrate the polarization of the beams.

generated and stabilized by three pairs of orthogonal Helmholtz coils centered on the cell. An internal 3-axis fluxgate sensor close to the cell acts as the feedback to three servo controllers, which actively adjust the current in each coil. A linearly polarized probe beam, resonant with the D_1 $F = 2 \rightarrow F'$ transition, propagates through the cell in the $\hat{y}$ direction. The RF coil is positioned above the cell along the $\hat{z}$ axis, and its frequency ω_{RF} is swept through the Larmor frequency ω_0 set by $\mathbf{B}_{Bias}$. This produces an oscillating magnetic field B_{RF}. Spin precession driven by B_{RF} is read out via Faraday rotation of the plane of polarization of the probe beam.[9] The polarization of the probe is then interrogated by a miniaturized polarimeter, consisting of a polarizing beam splitter (PBS) and two balanced photodiodes integrated on a printed circuit board. Finally, the electronic signal is processed with a lock-in amplifier (LIA), providing a phase-sensitive magnetic resonance, which carries information of the target properties.[10]

An image of a target object is built by acquiring a magnetic resonance at different positions, with each position defining a pixel. For each pixel, the RF-AM is translated and the RF coil frequency is swept from $\omega_0 - \Delta \rightarrow \omega_0 + \Delta$ where typically $\Delta/2\pi = 5$kHz. Resonances are built up with 25 frequency points per spectrum, and the in-phase (X) and out-of-phase (Y) components of the LIA are fitted to Lorentzian and dispersive lineshapes. The fitted lineshapes are then used to extract the amplitude, resonant frequency, and the linewidth Γ (FWHM) of the magnetic resonance. Near-resonant imaging[11] is utilized to produce more stable images with improved contrast. Briefly, the fitted resonances are used to track the resonant frequency at each pixel. X and Y at a desired detuning from resonance are extracted from the fitted lineshapes, and then, the radius $R = \sqrt{X^2 + Y^2}$ and phase $\Phi = \arctan(Y/X)$ at this detuning can be calulated. Two images are, therefore, built up, the R image and the Φ image.

The target object is a solid aluminum block of dimensions $108 \times 110 \times 12\,\text{mm}^3$ ($\text{W} \times \text{L} \times \text{H}$) with two 16 mm pilot-holes drilled symmetrically about the origin and separated by a distance of 36.7 mm. The target is placed on a plastic screen above the sensor head with a 0.1 mm standoff between the target and the top of the RF coil. This standoff distance was chosen to mimic the typical situation in manufacturing where the sensor is placed very close to the skin but we have also experimentally verified the efficacy of the technique in a standoff range of 0.1–2.5 mm. Eddy currents are excited in the target material, inducing secondary oscillating fields at the same frequency as the primary field. The summation of the primary and secondary fields gives rise to a change that is detectable by the RF-AM and by raster-scanning the RF-AM across the target, an image of the magnetic response can be built up.

Figures 2(a) and 2(b) show the R and Φ images of the target without conductive shielding, respectively. The origin of the target is roughly centered to the origin of the image, and a $90 \times 90\,\text{mm}^2$ image is built up with a pixel size of $1.5 \times 1.5\,\text{mm}^2$. The pilot-holes are

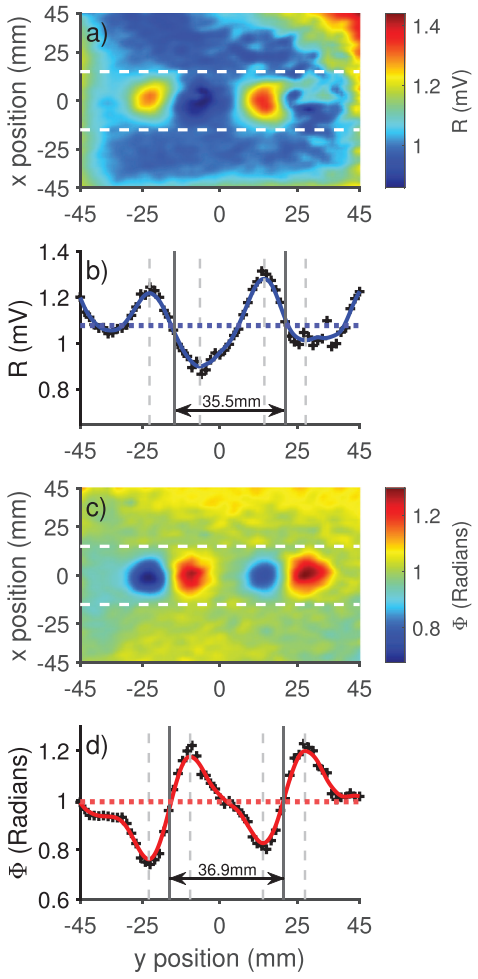

FIG. 2. R image (a) and Φ image (c) of the target plate without conductive shielding at 6 kHz. White dashed lines represent the bounds of the interpolation of the R image shown in (b) and of the Φ image shown in (d). For (b) and (d), the black crosses show the raw data points and the solid curves (blue and red, respectively) show smoothing spline interpolation of the data. The red and blue dashed lines in (b) and (d) show the mean of the R and Φ across the rest of the plate (outside the white dashed lines), respectively. The step of the translational stage was 1.5 mm. Gray dashed and black solid lines represent the peak/trough detection and the calculated pilot-hole centers, respectively. The images are smoothed by a convolution of the dataset with a nearest-neighbor Gaussian filter of radius 1 pixel.

© Author(s) 2022

clearly visible in both R and Φ. In the R image, boundary effects can be seen due to lower RF absorption as the magnetometer is close to the boundary of the target. The Φ image is interpolated within the bounds of the white dashed lines to produce the graph in Fig. 2(d), which shows how the phase of the magnetometer changes across the pilot-holes. The anti-symmetric shape of the phase change over the pilot-hole geometry can be explained by the B_{RF} reflecting off the brim of the pilot-hole and, therefore, adding an oscillating field component in the $\hat{y}$ direction.[12,13] Due to the pump being orientated along $\hat{x}$, the magnetometer is sensitive to B_{RF} in the $\hat{z}$ and $\hat{y}$ directions. This can be further explained by considering just one dimension. As the magnetometer scans across the pilot-hole, it crosses two boundaries. The field is reflected in opposite directions by the two boundaries, leading to the characteristic dispersive response shown in Fig. 2. The phase shape of the pilot-holes is compared to the average phase angle of the Φ image across the solid plate (red dashed line). At the pilot-hole center, the RF coil is equidistant from both edges of the pilot-hole and so the contributions of the reflected B_{RF} components are balanced and, thus, there is no change in the phase of the magnetometer due to the pilot-hole. The data are smoothed, and we utilize a peak detection algorithm in MATLAB (findpeaks) to detect the peak and trough of the characteristic shape of the pilot-hole detection. We define the pilot-hole center by taking the midpoint between the peak and trough and then calculate the separation between these values to localize the pilot-holes with respect to one another. As seen in Figs. 2(b) and 2(d), we apply the pilot-hole separation measurements to both R and Φ. We find that generally the Φ imaging produces a more accurate measurement as it is unaffected by the changing absorption of the primary field close to the boundaries. Using the Φ image amounts to a measurement of 36.9 ± 0.4 mm, which is in agreement with the real separation value to within 1 standard deviation.

For this work, the target is imaged with and without a conductive shield. The conductive shield is also made of aluminum and has dimensions of $108 \times 110 \times 0.41\ \text{mm}^3$ (W × L × H). B_{RF} penetrates the target material with its amplitude decaying with depth according to[11,14]

$$B_{RF}(z) = B_{RF}(0)e^{-z/\delta(\omega_{RF})}, \tag{1}$$

where $\delta(\omega_{RF})$ is the skin-depth of the aluminum, which can be described by[10]

$$\delta(\omega_{RF}) = \sqrt{\frac{2}{\omega_{RF}\sigma\mu}}\left[\sqrt{1+\left(\frac{\omega_{RF}\varepsilon}{\sigma}\right)^2}+\frac{\omega_{RF}\varepsilon}{\sigma}\right]^{1/2}, \tag{2}$$

where ε, μ, and σ are the electrical permittivity, the magnetic permeability, and the conductivity of the aluminum, respectively. Using different frequencies for B_{RF} allows tomographic imaging of the target, by penetrating to different depths and, hence, facilitates imaging behind barriers. We utilize a dual-frequency method of imaging[15] whereby two B_{RF} frequencies are chosen, the low-frequency to allow penetration of the shielding to image the target and a higher frequency to image the shielding alone. These two images are normalized to one another (by comparing the amplitude of the corners of the two images) and then subtracted to remove the effect of the shield from the image of the target. This improves the efficacy of the pilot-hole detection when close to boundaries and in situations where the shield is non-uniform, for example, where the shield is indented or embossed directly above the pilot-holes and if the shield contains defects that contribute to imaging noise on the surface. In our case, we choose the RF parameters as in Table I, which gives a difference in skin-depth that is comparable with the thickness of the aluminum shield of 0.41 mm. The imaging can be adjusted for the an arbitrary shield thickness by tuning the low-frequency [see Eq. (2)].

We now consider the case of through-skin imaging of the pilot-holes by utilizing the dual-frequency technique. We find that the shield introduces phase noise on the Φ image that significantly reduces the efficacy of the detection of the characteristic dispersive response of the pilot-holes. Hence, we utilize the R image for all shielded measurements. Figure 3 shows the imaging of the target when shielded by the 0.41 mm Al shield. The R image in (a) is taken at the high-frequency and, thus, gives the EMI profile of the shield piece, which has the same area as the target piece. The shield absorbs the RF and again the boundary effects appear at the peripherals of the image as the magnetometer approaches the edge of the shield. The R image in (b) is taken at the low-frequency and reveals the anti-symmetric shape across the pilot-holes. The boundary effects are also visible as image contains both the EMI of the shield and the target. By subtracting the high-frequency image from the low-frequency image, after appropriate normalization, we can obtain an image of the holes without the effect of the shield. The dashed blue line shows the average R across the solid plate. The shielded pilot-hole separation measurement is also extracted from the peak detection and yields 36.9 ± 0.7 mm. This is in agreement with the real separation value to within 1 standard deviation and demonstrates feasible submillimeter accuracy of through-skin pilot-hole localization.

We now address the issue of the robustness of the measurements with respect to a variation of the sensor operating parameters. Figure 4 shows the pilot-hole separation measurement as ω_{RF} is varied. The measured separation can be seen to be robust over the operating frequency range (5.5–100 kHz) and over multiple measurements, for both shielded and unshielded imaging. As an important fact, we notice that our approach does not require the skin and the strut to be in contact, unlike previously introduced techniques relying on transient-pulsed thermography[1] where thermal continuity is essential. This is very advantageous during the manufacturing process, as applied pressure on the skin to eliminate air gaps and produce physical contact between skin and target is not required. To demonstrate this, we image the target through the Al shield with a piece of a 1.5 mm thick insulating material (rubber) between the target and the conductive shield. The image, as shown in Fig. 5, has comparable contrast to that of Fig. 3(c) and yields a separation distance of 36.8 ± 0.7 mm. This indicates that effective through-skin imaging and pilot-hole localization can be obtained with a thermal and electrical insulator and that direct contact between the two parts is not a requirement.

TABLE I. RF frequencies chosen for the dual-frequency imaging. $\delta(\omega_{RF})$ is calculated using Eq. (2). The low-frequency has a skin-depth past the 0.41 mm Al shield, whereas the high-frequency does not.

	Frequency	$\delta(\omega_{RF})$
Low-frequency	6.5 kHz	0.81 mm
High-frequency	55 kHz	0.27 mm

© Author(s) 2022

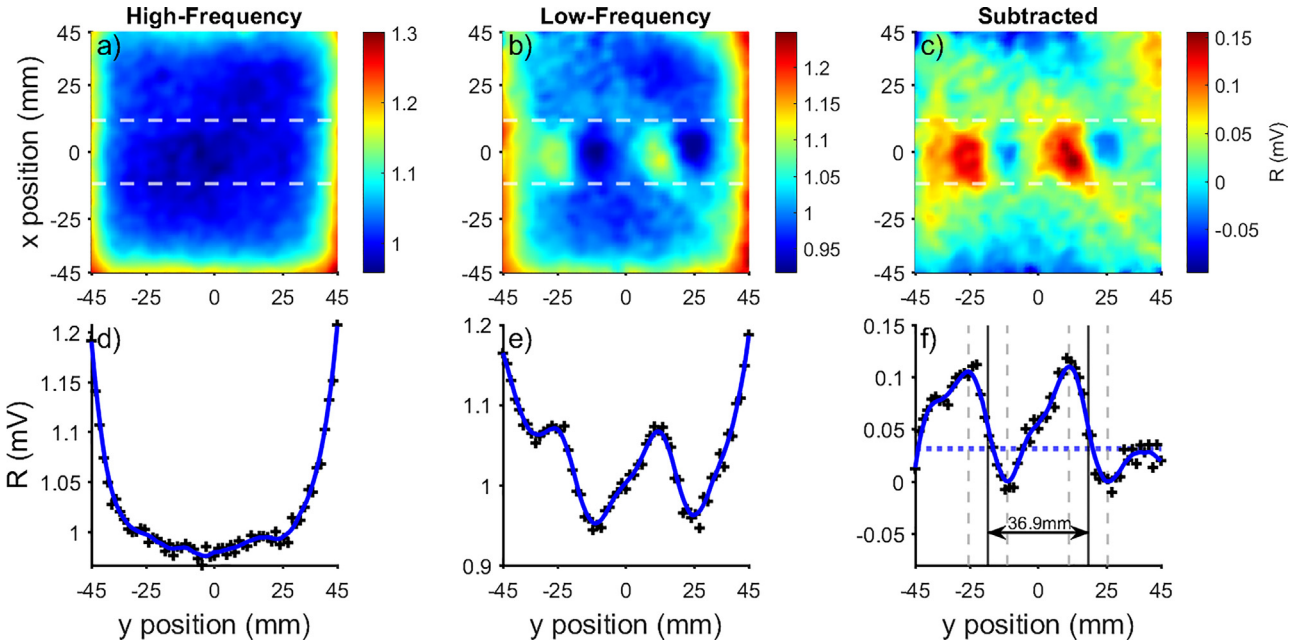

FIG. 3. *R* images of the target plate through the 0.41 mm Al shield at 55 (a), 6 kHz (b), and their dual-frequency subtraction image (c). White dashed lines in (a)–(c) represent the bounds of the interpolation of the *R* image shown in (d)–(f), respectively. The black crosses show the raw data points, and a smoothing spline interpolation is fit onto the top (blue). The blue dashed line in (f) shows the mean value of *R* outside of the white dashed lines in (c). Gray dashed and black solid lines represent the peak/trough detection and the calculated pilot-hole centers, respectively. The step of the translational stage was 1.5 mm. The images are smoothed by a convolution of the dataset with a nearest-neighbor Gaussian filter of radius 1 pixel.

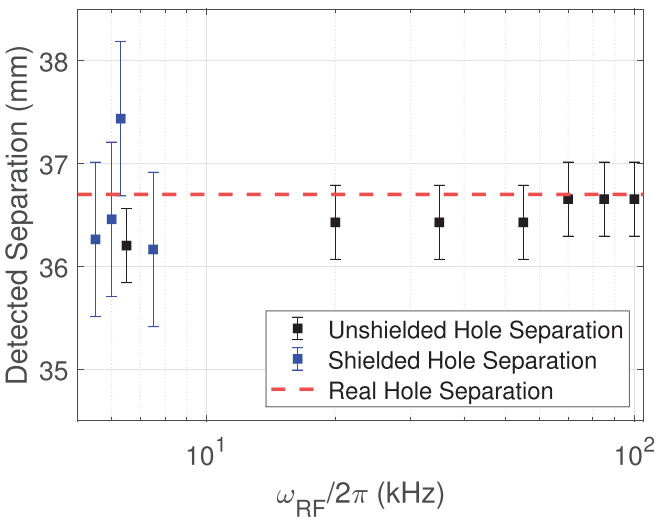

FIG. 4. Measured pilot-hole separation for dual-frequency imaging of the shielded target (blue squares) and single-frequency imaging of the unshielded target (black squares), with varying ω_{RF}, compared with the real pilot-hole separation of 36.7 mm (red dashed line). The error bar is the same for each unshielded measurement (black) and is based on 1 standard deviation of 10 successive unshielded measurements at 55 kHz. Similarly, the error bars for shielded measurements (blue) are all the same and based on 1 standard deviation of 10 successive shielded measurements at 6 kHz (blue).

In conclusion, this work addressed a widespread issue in manufacturing, and specifically in aircraft wings assembly: anchoring a metallic skin on a strut without visual access to the strut nor to eventual pilot-holes pre-drilled into it. The technique demonstrated here relies on electromagnetic induction imaging, with an atomic magnetometer, allowing for sufficiently low operation frequencies, which can penetrate through a shield leading to effective identification of the support strut and pilot-holes. Our technique compares well with existing solutions. With respect to transient-pulsed thermography,[1] our approach is advantageous as it does not require thermal contact

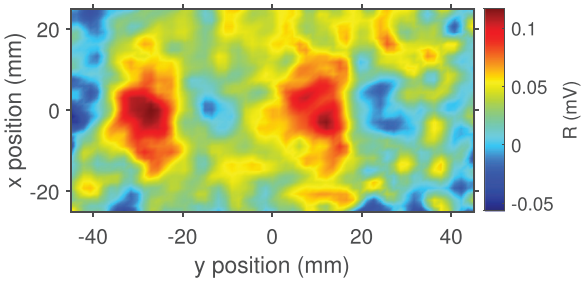

FIG. 5. Dual-frequency subtracted *R* image of the target with conductive shielding and a 1.5 mm layer of rubber separating the shield and target. The image is smoothed by a convolution of the dataset with a nearest-neighbor Gaussian filter of radius 1 pixel.

© Author(s) 2022

between skin and strut, therefore removing the requirement for perfect adhesion during the process. With respect to the approach involving the insertion of permanent magnets in the pilot-holes,[2] our approach does not require additional components to be temporarily inserted in the strut, thus allowing the entire anchoring process to be conducted from one side of the structure. The result presented in this work relied on a single sensor scanned over the skin. Further developments could involve the use of an array of four magnetometers,[16] so that the pilot-hole could be located while leaving access on the skin for the anchoring tool, speeding up the process. The localization could also be automated to detect the characteristic hole pattern in 2D with machine learning, which has previously been realized for EMI with atomic magnetometers for the classification of imaged objects.[17]

The authors thank Dr. Luca Marmugi for useful discussions. This work was funded by EPSRC Impact Acceleration Account (Grant No. EP/R511638/1).

AUTHOR DECLARATIONS

Conflict of Interest

The authors have no conflicts to disclose.

DATA AVAILABILITY

The data that support the findings of this study are available from the corresponding author upon reasonable request.

REFERENCES

[1]N. Avdelidis and D. P. Almond, "Transient thermography as a through skin imaging technique for aircraft assembly: Modelling and experimental results," Infrared Phys. Technol. **45**, 103–114 (2004).
[2]S. F. Pedigo, G. E. Georgeson, R. D. Rempt, G. L. Clark, and J. L. Hafenrichter, "Control system and method for a magnetic indexer for high accuracy hole drilling," U.S. patent 6,927,560 45 (2005).
[3]C. Deans, L. Marmugi, and F. Renzoni, "Through-barrier electromagnetic imaging with an atomic magnetometer," Opt. Express **25**, 17911–17917 (2017).
[4]A. Wickenbrock, N. Leefer, J. W. Blanchard, and D. Budker, "Eddy current imaging with an atomic radio-frequency magnetometer," Appl. Phys. Lett. **108**, 183507 (2016).
[5]D. Budker and M. Romalis, "Optical magnetometry," Nat. Phys. **3**, 227–234 (2007).
[6]W. Chalupczak, R. Godun, S. Pustelny, and W. Gawlik, "Room temperature femtotesla radio-frequency atomic magnetometer," Appl. Phys. Lett. **100**, 242401 (2012).
[7]I. M. Savukov, S. Seltzer, M. Romalis, and K. Sauer, "Tunable atomic magnetometer for detection of radio-frequency magnetic fields," Phys. Rev. Lett. **95**, 063004 (2005).
[8]C. Deans, Y. Cohen, H. Yao, B. Maddox, A. Vigilante, and F. Renzoni, "Electromagnetic induction imaging with a scanning radio frequency atomic magnetometer," Appl. Phys. Lett. **119**, 014001 (2021).
[9]S. Seltzer, "Developments in alkali-metal atomic magnetometry," Ph. D. dissertation (Princeton University, 2008).
[10]L. Marmugi and F. Renzoni, "Electromagnetic induction imaging with atomic magnetometers: Progress and perspectives," Appl. Sci. **10**, 6370 (2020).
[11]L. Marmugi, C. Deans, and F. Renzoni, "Electromagnetic induction imaging with atomic magnetometers: Unlocking the low-conductivity regime," Appl. Phys. Lett. **115**, 083503 (2019).
[12]P. Bevington, R. Gartman, and W. Chalupczak, "Magnetic induction tomography of structural defects with alkali–metal spin maser," Appl. Opt. **59**, 2276–2282 (2020).
[13]P. Bevington, R. Gartman, and W. Chalupczak, "Enhanced material defect imaging with a radio-frequency atomic magnetometer," J. Appl. Phys. **125**, 094503 (2019).
[14]P. A. Bottomley and E. R. Andrew, "Rf magnetic field penetration, phase shift and power dissipation in biological tissue: Implications for nmr imaging," Phys. Med. Biol. **23**, 630 (1978).
[15]B. J. Darrer, J. C. Watson, P. Bartlett, and F. Renzoni, "Magnetic imaging: A new tool for UK National Nuclear Security," Sci. Rep. **5**, 7944 (2015).
[16]C. Deans, L. Marmugi, and F. Renzoni, "Active underwater detection with an array of atomic magnetometers," Appl. Opt. **57**, 2346–2351 (2018).
[17]C. Deans, L. D. Griffin, L. Marmugi, and F. Renzoni, "Machine learning based localization and classification with atomic magnetometers," Phys. Rev. Lett. **120**, 033204 (2018).

© Author(s) 2022